Accurate numerical simulation of moisture front in porous material

Julien Berger, Suelen Gasparin, Denys Dutykh, Nathan Mendes

Julien Berger
Pontifical Catholic University of Paraná, Brazil

Suelen Gasparin
Pontifical Catholic University of Paraná, Brazil

Denys Dutykh
CNRS, Université Savoie Mont Blanc, France

Nathan Mendes
Pontifical Catholic University of Paraná, Brazil

Accurate numerical simulation of moisture front in porous material

arXiv.org / HAL

Last modified: March 26, 2017

Accurate numerical simulation of moisture front in porous material

Julien Berger*, Suelen Gasparin, Denys Dutykh, and Nathan Mendes

Abstract. When comparing measurements to numerical simulations of moisture transfer through porous materials a rush of the experimental moisture front is commonly observed in several works shown in the literature, with transient models that consider only the diffusion process. Thus, to overcome the discrepancies between the experimental and the numerical models, this paper proposes to include the moisture advection transfer in the governing equation. To solve the advection-diffusion or the so-called convection differential equation, it is first proposed two efficient numerical schemes and their efficiencies are investigated for both linear and nonlinear cases. The first scheme, Scharfetter–Gummel (SG), presents a Courant–Friedrichs–Lewy (CFL) condition but is more accurate and faster than the second scheme, the well-known Crank–Nicolson approach. Furthermore, the SG scheme has the advantages of being well-balanced and asymptotically preserved. Then, to conclude, results of the convective moisture transfer problem obtained with the SG numerical scheme are compared to experimental data from the literature. The inclusion of an advective term in the model may clearly lead to better results than purely diffusive models.

Key words and phrases: Advection-diffusion equation; numerical methods; benchmarking experimental data; Scharfetter–Gummel scheme; convective moisture transport; hygroscopic materials

MSC: [2010] 35R30 (primary), 35K05, 80A20, 65M32 (secondary)
PACS: [2010] 44.05.+e (primary), 44.10.+i, 02.60.Cb, 02.70.Bf (secondary)

Key words and phrases. Advection-diffusion equation; numerical methods; benchmarking experimental data; Scharfetter–Gummel scheme; convective moisture transport; hygroscopic materials.
* Corresponding author.

Contents

1. Introduction

Moisture in porous building elements can affect indoor air quality, thermal comfort and energy consumption/demand. excessive level of moisture may also damage the construction quality and their durability and can lead to mould growth on the inside surface [5, 18].

In order to predict those effects in buildings, moisture transfer models have been integrated in early nineties in simulation tools such as `Delphin` [3], `MATCH` [41], `MOIST` [6], `WUFI` [13], `Umidus` [31, 33] and `Blast` [28]. In the frame of the International Energy Agency Annex 41 , detailed models and their successful applications for accurate assessment of hygrothermal transfer in buildings have been reported [48].

1.1. Problem statement

Nevertheless, some discrepancies normally appear when comparing the results from numerical models and experimental data, as illustrated in Figure 1. A material, with an initial moisture content w_0, is submitted to an adsorption phase at ϕ_1 and then to a desorption phase at ϕ_2. Results of the simulation under estimate the adsorption process or over estimate the desorption process. In other terms, the experimental moisture front always rushes faster than the simulation results. Numerous studies state similar observations.

In [30] four cross-laminated timber wall assemblies were studied monitoring a test wall during one year period. The boundary conditions corresponded to outside weather and fixed in time for indoor side. The panels were initially wetted and their drying behaviour were analysed. Simulations were performed with the `WUFI` program (based on Kunzel diffusion model [24]), using material properties based on laboratory characterisation.

In [44, 45], spruce plywood and cellulose insulation were evaluated considering single-step change increase in humidity or adsorption and desorption cycle tests. The model used to compare the experimental data is based on moisture diffusion due to water vapour density or total gas pressure difference.

In [42], autoclaved and hemp concretes are used combined with various experimental designs. Data are compared with the Kunzel diffusion model [24]. The comparison reveals the same type of discrepancies, specially for the design operating four 24 hour steps of temperature and relative humidity.

In [19], gypsum boards were conditioned to adsorption and desorption cycles of $(30\% - 70\% - 30\%)$ relative humidity. The whole experiment was conducted for 48h under isothermal conditions. The numerical results, in terms of relative humidity, obtained with models from eight different institutions, were compared to experimental data. All the models predicted transient behaviour slower than experimental data.

In [9, 27] experiments were performed in a climatic chamber with hemp concrete samples. Slow and fast cycling tests of adsorption and desorption were done. The discrepancies between experimental data and model results were reduced by considering the hysteresis of the material moisture capacity. In [12], other hygrothermal data were provided for hemp

concrete and compared to a numerical model without hysteresis effect considerations. The conclusions underlined the good tendencies but nevertheless with some lack of accuracies. In [29], experiments for similar materials under climatic variations were performed. Influence of material properties and convective coefficients were investigated to reduce the discrepancies with experimental data.

Some experimental designs were also operated at the building scale. In [26, 38], a wooden-frame house was instrumented. Vapour was generated during certain periods. The comparison with the numerical model was during and after those periods and some discrepancies were observed in the transient behaviour. An experimental benchmark is presented in [47], using calcium silicate boards submitted to five adsorption and desorption cycles ($50\% - 70\% - 50\%$). The model used for comparison included two sub-models considering coupled heat and moisture transfer equations in the material and in the air within the climatic chamber.

All those studies highlighted slower transient behaviour of the results obtained by numerical models comparing to experimental data. The observations are particularly valuable for hygroscopic materials. The models are based on the coupled heat and moisture diffusion in porous materials.

1.2. Objectives of the paper

Some attempts have been done to reduce those discrepancies. Among others, in [9, 25, 27], the hysteresis of the sorption material capacity was considered. In [35] a non-FICKIAN moisture diffusion model was proposed for thermally modified wood. A possible explanation of the slower transient behaviour of the numerical results is the absence of advection transfer in the proposed model. When the advective and diffusive fluxes have the same direction, the advection mechanism increases the moisture front velocity. Hygroscopics materials such as wood fibre board, gypsum board and aerated cellular concreted have a larger air permeability, almost three orders of magnitude higher, if compared with the concrete one [23]. Some numerical models have been developed considering moisture advection [4]. However, to the knowledge of the authors, no comparison with experimental studies of adsorption/desorption cycles for building materials have been accomplished.

Thus, the objectives of this paper are basically two. First, it aims at analysing the numerical schemes to solve an advective-diffusive problem or the so-called convective moisture transfer in porous materials, represented by a model proposed in Section 2. After a brief recall of the fundamentals and objectives of numerical methods, the CRANK–NICOLSON and the SCHARFETTER–GUMMEL schemes are then described. The primer has been extensively used to solve advective-diffusive equation as for instance in [37]. The latter is a relatively innovative approach, despite being firstly proposed in 1969, and presents several advantages that will be discussed for both linear and nonlinear problems. Then, the second objective is to illustrate the influence of the moisture convection hypothesis on the comparison with the experimental results. Thus, in the last section, the results of the SCHARFETTER–GUMMEL scheme are compared to an isothermal experiment from [19].

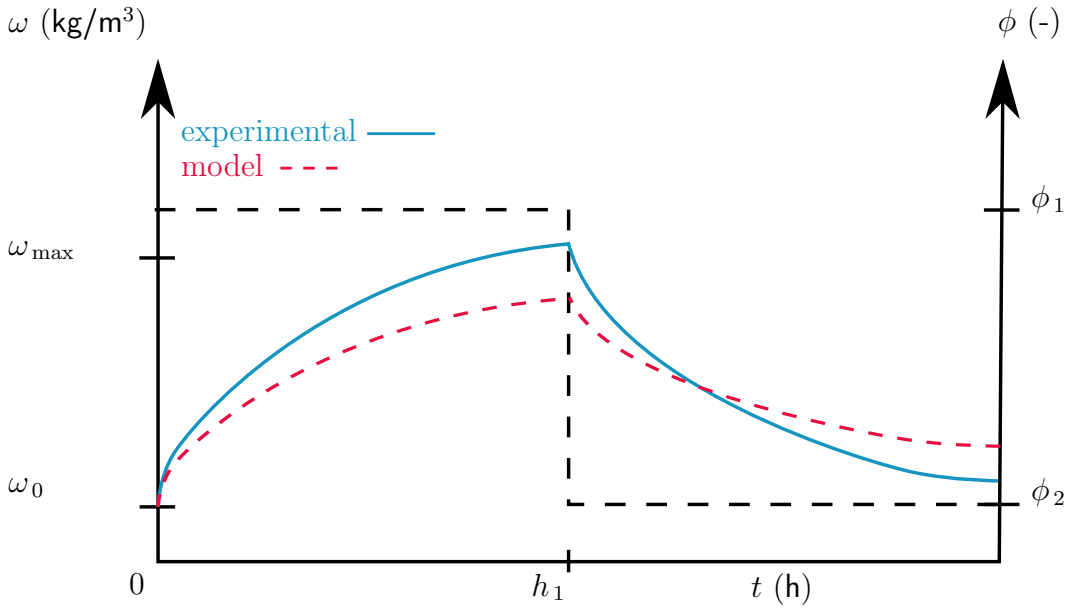

Figure 1. *Illustration of the discrepancies observed when comparing experimental data to results from numerical model of moisture transfer in porous material.*

2. Moisture transfer in porous materials by diffusion and advection

The physical problem involves one-dimension moisture convection through a porous material defined by the spatial domain $\Omega_x = [0, L]$. The moisture transfer occurs due to capillary migration, vapour diffusion and advection of the vapour phase. The physical problem can be formulated as [4, 20, 46]:

$$\frac{\partial \rho_{l+v}}{\partial t} = \frac{\partial}{\partial x}\left(k_l \frac{\partial P_c}{\partial x} + k_v \frac{\partial P_v}{\partial x} \right) - \frac{\partial}{\partial x}\left(\frac{P_v}{R_v\, T} v \right), \tag{2.1}$$

where ρ_{l+v} is the volumetric moisture content of the material, k_v and k_l, the vapour and liquid permeabilities, P_v, the vapour pressure, T, the temperature, v, the air velocity and, R_v, the water vapour gas constant. Eq. (2.1) can be written using the vapour pressure P_v as the driving potential. For this, we consider the physical relation, known as the Kelvin equation, between P_v and P_c:

$$P_c = R_v T \ln\left(\frac{P_v}{P_s(T)} \right),$$
$$\frac{\partial P_c}{\partial P_v} = \frac{R_v T}{P_v}.$$

Thus we have:

$$\frac{\partial P_c}{\partial x} \;=\; \frac{\partial P_c}{\partial P_v}\,\frac{\partial P_v}{\partial x} \;+\; \frac{\partial P_c}{\partial T}\,\frac{\partial T}{\partial x}\,.$$

The temperature remains the same at the boundaries. Even if heat transfer occurs in the material due to latent heat evaporation, the temperature variations in the material are assumed negligible. Thus, the second right-hand term vanishes and we obtain:

$$\frac{\partial P_c}{\partial x} \;=\; \frac{R_v\,T}{P_v}\,\frac{\partial P_v}{\partial x}\,.$$

In addition, we have:

$$\frac{\partial \rho_{l+v}}{\partial t} \;=\; \frac{\partial \rho_{l+v}}{\partial \phi}\,\frac{\partial \phi}{\partial P_v}\,\frac{\partial P_v}{\partial t} \;+\; \frac{\partial \rho_{l+v}}{\partial T}\,\frac{\partial T}{\partial t}\,.$$

Under isothermal conditions, the second right-hand term of the equation above also vanishes. Considering the relation $\rho_{l+v} \;=\; \mathrm{f}(\phi) \;=\; \mathrm{f}(P_v, T)$, obtained from material properties and from the relation between the vapour pressure P_v and the relative humidity ϕ, we get:

$$\frac{\partial \rho_{l+v}}{\partial t} \;=\; \mathrm{f}'(P_v)\,\frac{1}{P_s}\,\frac{\partial P_v}{\partial t}\,.$$

For the advection term of Eq. (2.1), with the assumption of isothermal conditions and constant air velocity v, we can write:

$$\frac{\partial}{\partial x}\left(\frac{P_v}{R_v\,T}\,\mathsf{v}\right) \simeq \frac{\mathsf{v}}{R_v\,T}\,\frac{\partial P_v}{\partial x}\,.$$

Eq. (2.1) can be therefore rewritten as:

$$\mathrm{f}'(P_v)\,\frac{1}{P_s}\,\frac{\partial P_v}{\partial t} \;=\; \frac{\partial}{\partial x}\left[\left(k_l\,\frac{R_v T}{P_v} \;+\; k_v\right)\frac{\partial P_v}{\partial x}\right] \;-\; \frac{v}{R_v\,T}\,\frac{\partial P_v}{\partial x}\,. \tag{2.2}$$

The material properties $\mathrm{f}'(P_v)$, k_l and k_v depend on the vapour pressure P_v. We denote $d_m \;=\; k_l\,\dfrac{R_v T}{P_v} \;+\; k_v$ the global moisture transport coefficient and $c_m \;=\; \mathrm{f}'(P_v)\,\dfrac{1}{P_s}$ the moisture storage coefficient. Thus, Eq. (2.2) becomes:

$$c_m\,\frac{\partial P_v}{\partial t} \;=\; \frac{\partial}{\partial x}\left[d_m\,\frac{\partial P_v}{\partial x}\right] \;-\; \frac{\mathsf{v}}{R_v\,T}\,\frac{\partial P_v}{\partial x}\,. \tag{2.3}$$

At the material bounding surfaces, Robin-type boundary conditions are considered:

$$d_m\,\frac{\partial P_v}{\partial x} \;=\; h_v^{\mathrm{L}}\cdot\left(P_v \;-\; P_v^{\mathrm{L}}\right) \;-\; g_l^{\mathrm{L}}\,, \qquad x \;=\; 0\,, \tag{2.4}$$

$$-d_m\,\frac{\partial P_v}{\partial x} \;=\; h_v^{\mathrm{R}}\cdot\left(P_v \;-\; P_v^{\mathrm{R}}\right)\,, \qquad x \;=\; L\,, \tag{2.5}$$

where P_v^{L} and P_v^{R} are the vapour pressure of the ambient air, g_l^{L} are the liquid flow (driving rain) at the two bounding surfaces. We consider a uniform vapour pressure distribution as

initial condition:

$$P_v = P_v^i, \qquad t = 0. \tag{2.6}$$

While performing a mathematical and numerical analysis of a given practical problem, it is of capital importance to obtain a unitless formulation of governing equations, due to a number of good reasons. First of all, it enables to determine important scaling parameters (Biot numbers for instance). Henceforth, solving one dimensionless problem is equivalent to solve a whole class of dimensional problems sharing the same scaling parameters. Then, dimensionless equations allow to estimate the relative magnitude of various terms, and thus, eventually to simplify the problem using asymptotic methods [34]. Finally, the floating point arithmetics is designed such as the rounding errors are minimal if you manipulate the numbers of the same magnitude [22]. Moreover, the floating point numbers have the highest density in the interval $(0, 1)$ and their density decays exponentially when we move further away from zero. So, it is always better to manipulate numerically the quantities at the order of $\mathcal{O}(1)$ to avoid severe round-off errors and to likely improve the conditioning of the problem in hands.

Therefore, the following dimensionless quantities are defined:

$$u = \frac{P_v}{P_v^i}, \qquad u^{\mathrm{R}} = \frac{P_v^{\mathrm{R}}}{P_v^i}, \qquad u^{\mathrm{L}} = \frac{P_v^{\mathrm{L}}}{P_v^i}, \qquad x^\star = \frac{x}{L},$$

$$t^\star = \frac{t}{t^0}, \qquad c_m^\star = \frac{c_m \cdot L^2}{d_m^0 \cdot t^0}, \qquad d_m^\star = \frac{d_m}{d_m^0}, \qquad \mathrm{Pé} = \frac{\mathsf{v} \cdot L}{R_v \cdot T \cdot d_m^0},$$

$$\mathrm{Bi}_v^{\mathrm{L}} = \frac{h_v^{\mathrm{L}} \cdot L}{d_m^0}, \qquad \mathrm{Bi}_v^{\mathrm{R}} = \frac{h_v^{\mathrm{R}} \cdot L}{d_m^0}, \qquad g_l^{\star \mathrm{L}} = \frac{g_l^{\mathrm{L}} \cdot L}{d_m^0 \cdot P_v^i}.$$

In this way, the dimensionless governing equations are then written as:

$$c_m^\star \frac{\partial u}{\partial t^\star} = \frac{\partial}{\partial x^\star}\left(d_m^\star \frac{\partial u}{\partial x^\star} \right) - \mathrm{Pé} \frac{\partial u}{\partial x}, \qquad t^\star > 0, \qquad x^\star \in \left[0, 1\right], \tag{2.7a}$$

$$d_m^\star \frac{\partial u}{\partial x^\star} = \mathrm{Bi}_v^{\mathrm{L}} \cdot \left(u - u^{\mathrm{L}} \right) - g_l^{\star \mathrm{L}}, \qquad t^\star > 0, \qquad x^\star = 0, \tag{2.7b}$$

$$-d_m^\star \frac{\partial u}{\partial x^\star} = \mathrm{Bi}_v^{\mathrm{R}} \cdot \left(u - u^{\mathrm{R}} \right), \qquad t^\star > 0, \qquad x^\star = 1, \tag{2.7c}$$

$$u = 1, \qquad t^\star = 0, \qquad x^\star \in \left[0, 1\right]. \tag{2.7d}$$

3. Numerical schemes

As the material properties varies with the field, it is not possible to compute an analytical solution of the problem. Therefore, one must use numerical approach, based here on finite differences. It considers a discretisation of the time and space grids with a local approximation of the derivatives. The main issues of a numerical scheme is (i) its global

error and (ii) the appropriate behaviour of the solution to represent the physical phenomenon. The primer is quantified by the accuracy of the method, related to the order order of truncation when approximating the derivatives. The second is associated to with the absolute stability of the scheme. A stable scheme avoids to compute a wrong solution. Moreover, an interesting aspect of a numerical scheme is the CPU time, corresponding to the physical clock-time to compute the solution of the problem. Interested readers are invited to consult [17, 32] for more details.

In order to describe numerical schemes, consider a uniform discretisation of the interval $\Omega_x \rightsquigarrow \Omega_h$:

$$\Omega_h = \bigcup_{j=0}^{N-1} [\, x_j,\, x_{j+1} \,], \qquad x_{j+1} - x_j \equiv \Delta x, \quad \forall j \in \{0, 1, \ldots, N-1\}.$$

The time layers are uniformly spaced as well $t^n = n\,\Delta t$, $\Delta t = \text{const} > 0$, $n = 0, 1, 2, \ldots, N_t$. The values of function $u(x, t)$ in discrete nodes will be denoted by $u_j^n \overset{\text{def}}{:=} u\,(x_j, t^n)$.

For the sake of simplicity and without loosing the generality, the numerical schemes are explained for the one-dimensional linear convection equation written as:

$$\frac{\partial u}{\partial t} + \frac{\partial J}{\partial x} = 0, \qquad t > 0, \qquad x \in \big[\, 0, 1 \,\big], \tag{3.1a}$$

$$J = a\,u - \nu \frac{\partial u}{\partial x}, \tag{3.1b}$$

where $u(x, t)$, $x \in \Omega$, $t > 0$, is the field of interest, $\nu = \dfrac{d_m}{c_m} > 0$ the diffusion coefficient and $a = \dfrac{\text{Pé}}{c_m} \in \mathbb{R}$ the advection coefficient. The boundary conditions are also written using a simplified notation:

$$\frac{\partial u}{\partial x} = \text{Bi} \cdot \big(\, u - u^{\text{L}} \big) - \text{g}, \qquad x = 0,$$

$$-\frac{\partial u}{\partial x} = \text{Bi} \cdot \big(\, u - u^{\text{R}} \big), \qquad x = 1.$$

In addition, for the sake of clarity, the upper-script $\star$ standing for dimensionless parameter, is no longer used.

3.1. The Crank–Nicolson scheme

The method proposed by Crank & Nicolson (CN) [10] is widely popular in many applications, and it is known specially for its stability. In this case, the CN scheme is applied to the convection–diffusion equation (3.1a):

$$\frac{u_j^{n+1} - u_j^n}{\Delta t} + \frac{1}{\Delta x}\left[J_{j+\frac{1}{2}}^{n+\frac{1}{2}} - J_{j-\frac{1}{2}}^{n+\frac{1}{2}} \right] = 0, \quad j = 1, \ldots, N-1, \qquad n \geqslant 0, \tag{3.2}$$

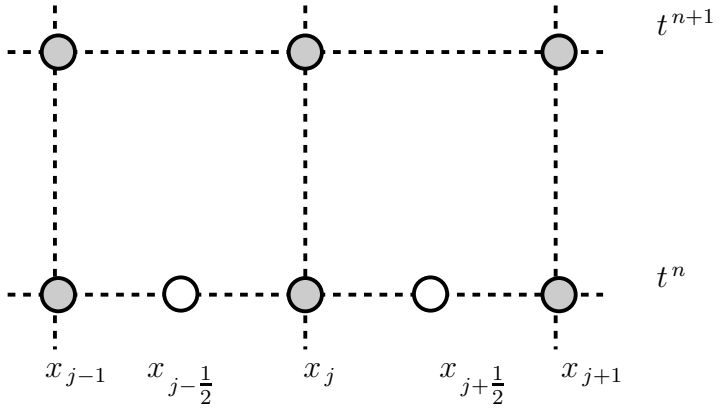

Figure 2. *Stencil of the numerical schemes.*

in which,

$$J^{n+\frac{1}{2}}_{j\pm\frac{1}{2}} \;=\; \frac{1}{2}\left(J^{n}_{j\pm\frac{1}{2}} \;+\; J^{n+1}_{j\pm\frac{1}{2}}\right). \tag{3.3}$$

The flux J is defined using the upwind scheme [36]:

$$J^{n}_{j+\frac{1}{2}} \;=\; \left\{\begin{matrix} a\,u^{n}_{j}\,, & a \geqslant 0 \\ a\,u^{n}_{j+1}\,, & a < 0 \end{matrix}\right\} \;-\; \nu\,\frac{\left(u^{n}_{j+1} \;-\; u^{n}_{j}\right)}{\Delta x}\,. \tag{3.4}$$

Parameter a is related to the advection transfer mechanisms in Eq. (3.1a). Thus, an upwind scheme defines the flux J according to the sense of the advection transfer. If $a \;\geqslant\; 0$, the advective flux is directed from x_j to $x_{æ+1}$ and the flux is therefore approximated using u^{n}_{j}.

Substituting Eq. (3.4) into Eq. (3.2), we obtain a discrete dynamical system:

$$\begin{aligned}\left[1 \;+\; 2\,\lambda \;+\; \gamma\,(\mathrm{b}^{+} \;-\; \mathrm{b}^{-})\right]u^{n+1}_{j} \;-\; (\lambda \;-\; \gamma\,\mathrm{b}^{-})\,u^{n+1}_{j+1} \;-\; (\gamma\,\mathrm{b}^{+} \;+\; \lambda)\,u^{n+1}_{j-1} \;=\\ \left[1 \;-\; 2\,\lambda \;-\; \gamma\,(\mathrm{b}^{+} \;-\; \mathrm{b}^{-})\right]u^{n}_{j} \;+\; (\lambda \;-\; \gamma\,\mathrm{b}^{-})\,u^{n}_{j+1} \;+\; (\gamma\,\mathrm{b}^{+} \;+\; \lambda)\,u^{n}_{j-1}\,,\end{aligned} \tag{3.5}$$

where

$$\lambda \;=\; \frac{\nu\,\Delta t}{2\,\Delta x^{2}}\,, \qquad \gamma \;=\; \frac{a\,\Delta t}{2\,\Delta x} \qquad \text{and} \qquad \mathrm{b}^{\pm} \;=\; \frac{1 \;\pm\; \mathrm{sign}(a)}{2}\,.$$

This scheme is $\mathcal{O}(\Delta t^{2} \;+\; \Delta x)$ accurate and unconditionally stable (at least for linear problems). The loose of one order in Δx is due to the advection. If Pé $\;=\;$ 0, than $\mathcal{O}(\Delta t^{2} \;+\; \Delta x^{2})$. Its stencil is illustrated in Figure 2.

3.2. The Scharfetter–Gummel scheme

Using the Crank–Nicolson approach, the numerical flux J from Eq. (3.1a) is approximated by central differences. Assuming J constant on the dual cell $\left[x_j^n,\, x_{j+1}^n\right]$, Scharfetter and Gummel start from the fact that the numerical flux at each interface $x_{j+\frac{1}{2}}$ can be computed giving the following boundary-value problem [14, 16, 43]:

$$J_{j+\frac{1}{2}}^n = a\,u - \nu\frac{\partial u}{\partial x}, \qquad \forall x \in \left[x_j^n,\, x_{j+1}^n\right]; \tag{3.6a}$$

$$u = u_j^n, \qquad x = x_j^n; \tag{3.6b}$$

$$u = u_{j+1}^n, \qquad x = x_j^{n+1}. \tag{3.6c}$$

An advantageous feature is that solution of Eq. (3.6) corresponds to the solution of the Poincaré–Steklov operator,

$$\mathcal{S} : (u_j^n,\, u_{j+1}^n) \mapsto J_{j+\frac{1}{2}}^n$$

and can be expressed as:

$$J_{j+\frac{1}{2}}^n = \frac{\nu}{\Delta x}\left[-\mathcal{B}\left(\frac{a\,\Delta x}{\nu}\right)u_j^{n+1} + \mathcal{B}\left(-\frac{a\,\Delta x}{\nu}\right)u_j^n\right], \tag{3.7}$$

where $\mathcal{B}$ corresponds to the Bernoulli function defined by

$$\mathcal{B}(z) \overset{\text{def}}{:=} \frac{z}{\mathrm{e}^z - 1}.$$

Therefore, given Eq. (3.7) and the Poincaré–Steklov operator, the Scharfetter–Gummel numerical scheme is written as:

$$\frac{u_j^{n+1} - u_j^n}{\Delta t} + \frac{1}{\Delta x}\left[\mathcal{S}(u_{j+1}^n, u_j^n) - \mathcal{S}(u_j^n, u_{j-1}^n)\right] = 0.$$

Finally, the scheme yields to:

$$\begin{aligned}\Big\{1 + \lambda\big[\mathcal{B}(-\theta) + \mathcal{B}(\theta)\big]\Big\}u_j^{n+1} - \lambda\,\mathcal{B}(\theta)\,u_{j+1}^{n+1} - \lambda\,\mathcal{B}(-\theta)\,u_{j-1}^{n+1} \\ = \Big\{1 - \lambda\big[\mathcal{B}(-\theta) + \mathcal{B}(\theta)\big]\Big\}u_j^n + \lambda\,\mathcal{B}(\theta)\,u_{j+1}^n + \lambda\,\mathcal{B}(-\theta)\,u_{j-1}^n,\end{aligned}$$

where

$$\lambda \overset{\text{def}}{:=} \frac{\nu\,\Delta t}{2\,\Delta x^2} \qquad \text{and} \qquad \theta \overset{\text{def}}{:=} \frac{a\,\Delta x}{\nu}.$$

Another interesting point is that, considering Eq. (3.6), the exact interpolation of solution $u(x)$ can be computed for $x \in \left[x_j^n,\, x_{j+1}^n\right]$ by:

$$u(x) = \frac{1}{a}\,J_{j+\frac{1}{2}}^n + \frac{\left(u_j^n - u_j^{n+1}\right)}{\mathrm{e}^{\frac{a\,x_j}{\nu}} - \mathrm{e}^{\frac{a\,x_{j+1}}{\nu}}}\,\mathrm{e}^{\frac{a\,x}{\nu}}.$$

For the nodes at the boundary surface, $j = \{1, N\}$, the flux $J_{\frac{1}{2}}$ is solution of

$$\begin{aligned} J_{\frac{1}{2}}^n &= a\,u - \nu\frac{\partial u}{\partial x}, && \forall x \in \left[0, x_1^n\right]; \\ \frac{\partial u}{\partial x} &= \mathrm{Bi}\cdot\left(u - u^{\mathrm{L}}\right) - \mathrm{g}, && x = 0; \\ u &= u_1^n, && x = x_1^n. \end{aligned}$$

and $J_{N+\frac{1}{2}}$ of

$$\begin{aligned} J_{N+\frac{1}{2}}^n &= a\,u - \nu\frac{\partial u}{\partial x}, && \forall x \in \left[x_N^n, 1\right]; \\ u &= u_N^n, && x = x_N^n; \\ -\frac{\partial u}{\partial x} &= \mathrm{Bi}\cdot\left(u - u^{\mathrm{R}}\right), && x = 1. \end{aligned}$$

Thus, we have:

$$J_{\frac{1}{2}}^n = a\,\frac{\left(\mathrm{Bi} - a\right)u_1^n - \left(\mathrm{Bi}\,u^{\mathrm{L}} + g\right)\mathrm{e}^{\frac{a\,\Delta x}{2\,\nu}}}{\mathrm{Bi} - a - \mathrm{Bi}\,\mathrm{e}^{\frac{a\,\Delta x}{2\,\nu}}},$$

$$J_{N+\frac{1}{2}}^n = a\,\frac{\mathrm{Bi}\,u^{\mathrm{R}} - \left(\mathrm{Bi} - a\right)u_N^n\,\mathrm{e}^{\frac{a\,\Delta x}{2\,\nu}}}{\mathrm{Bi} - \left(\mathrm{Bi} - a\right)\mathrm{e}^{\frac{a\,\Delta x}{2\,\nu}}}.$$

The stencil is illustrated in Figure 2. The important feature of the Scharfetter–Gummel numerical scheme is well balanced as well as asymptotically preserved. The limiting behaviour of the discrete equations is correct independently from grid parameters:

$$\lim_{a\,\to\,0} J_{j+\frac{1}{2}}^n = -\,\nu\,\frac{u_{j+1}^n - u_j^n}{\Delta x},$$

$$\lim_{\nu\,\to\,0} J_{j+\frac{1}{2}}^n = \begin{cases} a\,u_j^n, & a \leqslant 0, \\ a\,u_{j+1}^n, & a > 0. \end{cases}$$

Furthermore, the computation of $J_{j+\frac{1}{2}}^n$ is exact and it gives an excellent approximation of the physical phenomena. The only approximation is done when assuming $J_{j+\frac{1}{2}}^n$ constant in the interval $\left[x_{j-\frac{1}{2}}^n, x_{j+\frac{1}{2}}^n\right]$. In addition, when the steady state is reached, the solution computed with the scheme becomes exact [21]. Interested readers may consult [14, 16, 36] for recent works on the Scharfetter–Gummel scheme.

On the contrary to the Crank–Nicolson, the Scharfetter–Gummel scheme is not unconditionally stable. It has a stability limitation. It means that the scheme can compute

a solution when the so called standard Courant–Friedrichs–Lewy (CFL) condition is respected. In the linear case, the CFL condition of the Scharfetter–Gummel scheme is given by [15]:

$$\Delta t \, \frac{\mathrm{Pé}}{d_m^\star} \, \tanh\left(\frac{\mathrm{Pé} \, \Delta x}{2 \, d_m^\star} \right)^{-1} \leqslant \Delta x \, \frac{c_m^\star}{d_m^\star} \, . \tag{3.8}$$

If the spatial grid is refined, $\lim\limits_{\Delta x \to 0} \tanh(\Delta x) = \Delta x$, and the CFL condition starts to become quadratic $\Delta t \leq C_1 \cdot \Delta x^2$. However, if the spatial grid is large, $\lim\limits_{\Delta x \to 1} \tanh(\Delta x) = 1$ and the CFL condition yields to $\Delta t \leq C_2 \cdot \Delta x$. For these reasons, the values of Δx have to be in a closed interval, depending on the material properties.

3.3. Comparison of numerical schemes

A primary comparison of the numerical schemes can be done by computing the $\mathcal{L}_2$ error between the solution $u_{\,\mathrm{num}}$ and a reference solution $u_{\,\mathrm{ref}}$:

$$\varepsilon \overset{\mathrm{def}}{:=} \sqrt{\frac{1}{N_t \, N_x} \sum_{n=1}^{N_t} \sum_{j=1}^{N_x} \Big(u_{\mathrm{num}}(x_j, t_n) \; - \; u_{\mathrm{ref}}(x_j, t_n) \Big)^2} \, . \tag{3.9}$$

The reference solution is computed using the `Matlab` open source package *Chebfun* [11]. Using the function `pde23t`, it enables to compute a numerical solution of a partial derivative equation using the Chebyshev functions. The $\mathcal{L}_2$ error can also be computed along the space or time domains, according to:

$$\varepsilon(x) \overset{\mathrm{def}}{:=} \sqrt{\frac{1}{N_t} \sum_{n=1}^{N_t} \Big(u_{\mathrm{num}}(x, t_n) \; - \; u_{\mathrm{ref}}(x, t_n) \Big)^2} \, ,$$

$$\varepsilon(t) \overset{\mathrm{def}}{:=} \sqrt{\frac{1}{N_x} \sum_{j=1}^{N_x} \Big(u_{\mathrm{num}}(x_j, t) \; - \; u_{\mathrm{ref}}(x_j, t) \Big)^2} \, .$$

4. Numerical application: linear case

A first case of linear moisture transfer is considered to validate the solutions obtained by the Crank–Nicolson and Scharfetter–Gummel numerical schemes. The dimensionless properties of the material are equal to $d_m^\star = 1$ and $c_m^\star = 47$. The Péclet Number is taken as $\mathrm{Pe} = 20$. The final simulation time is fixed to $\tau^\star = 120$. The external and internal Biot numbers are $\mathrm{Bi}_v^{\mathrm{L}} = 2.5$ and $\mathrm{Bi}_v^{\mathrm{R}} = 1$, respectively. The boundary

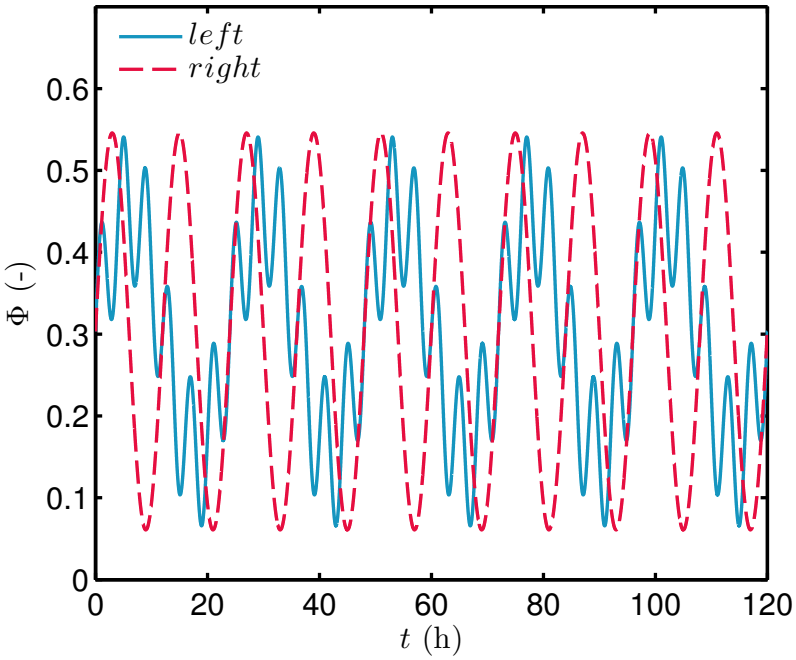

Figure 3. *Boundary conditions.*

conditions were described as:

$$u^{\mathrm{L}}(t^\star) = 1 + \frac{1}{2}\sin\left(\frac{2\pi\, t^\star}{24}\right) + \frac{3}{10}\sin\left(\frac{2\pi\, t^\star}{4}\right),$$
$$u^{\mathrm{R}}(t^\star) = 1 + \frac{4}{5}\sin\left(\frac{2\pi\, t^\star}{12}\right).$$

From a physical point of view, the numerical values correspond to a material length $L = 0.1\ \mathsf{m}$. The moisture properties are $d_m = 3\cdot 10^{-10}\ \mathsf{s}$ and $c_m = 1.8\cdot 10^{-4}\ \mathsf{kg/m^3/s}$, corresponding approximately to the wood fibre from [39]. The initial vapour pressure in the material is considered uniform $P_v^i = 7.1\cdot 10^2\ \mathsf{Pa}$, corresponding to a relative humidity of 30 %. The reference time is $t^0 = 1\ \mathsf{h}$, thus the total time of simulation corresponds to 120 hours, or five days. The boundary conditions, represented by the relative humidity ϕ are given in Figure 3. The sinusoidal variations oscillate between dry and moist state during 120 hours. The convective vapour coefficients are set to $8\cdot 10^{-9}\ \mathsf{s/m}$ and $3.5\cdot 10^{-9}\ \mathsf{s/m}$ for the left and right boundary conditions, respectively.

The solution of the problem has been first computed for a discretisation $\Delta x = 5\cdot 10^{-4}$ and $\Delta t = 10^{-3}$. The physical phenomena are thus well represented, as illustrated in Figure 4(a) with the time evolution of the vapour pressure at $x = 0$. The variations follow the ones of the left boundary conditions. It can be noted a good agreement between the two numerical schemes with the reference. Furthermore, the vapour pressure profile is shown in Figure 4(b) for $t = 19\ \mathsf{h}$ and $t = 77\ \mathsf{h}$.

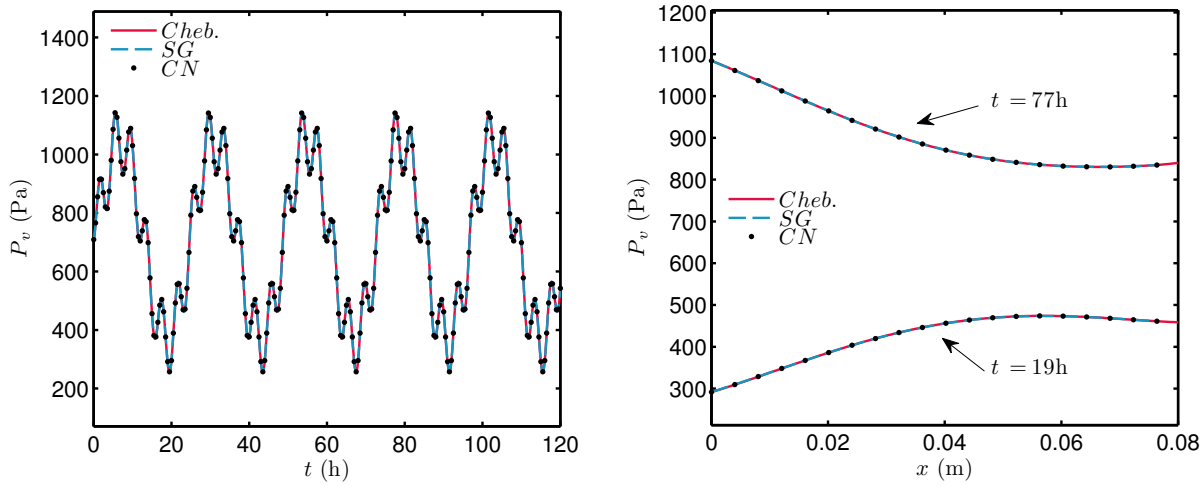

(a) (b)

Figure 4. *Vapour pressure time evolution at* $x = 0$ m *(a) and profiles for* $t \in \{19, 77\}$ h *(b).*

The reference solution has been computed using the `Matlab` open source toolbox *Chebfun* [11]. Using the function `pde23t`, it enables to compute a numerical solution of a partial derivative equation using the CHEBYSHEV functions. Both CRANK–NICOLSON and SCHARFETTER–GUMMEL numerical schemes give accurate results as illustrated with the L_2 error calculated as a function of x in Figure 5(b) and calculated as a function of t in Figure 5(a). In these figures it is possible to verify that the order of accuracy of both schemas is $\mathcal{O}(\Delta t^2 + \Delta x)$. In this case study, it was considered $\Delta x = 5 \cdot 10^{-4}$ and $\Delta t = 10^{-3}$, which leads to an order of accuracy of $\mathcal{O}(10^{-6} + 5 \cdot 10^{-4}) \sim \mathcal{O}(10^{-4})$.

A numerical analysis of the behaviour of the two numerical schemes has been carried out for different values of the temporal discretisation Δt and spatial discretisation Δx. The spatial discretisation is maintained to $\Delta x = 10^{-4}$ and $\Delta x = 10^{-2}$. Results of L_2 error can be seen in Figure 6(a) and Figure 6(b). It can be seen in Figure 6(a) that the error has a minimum value when Δt varies because the order of error of Δx is higher. After that minimum value, the error gets proportional to a constant multiplied by the order of $\mathcal{O}(\Delta t^2)$. Both figures confirm that the errors of the SCHARFETTER–GUMMEL and CRANK–NICOLSON schemes are proportional to $\mathcal{O}(\Delta t^2)$ and $\mathcal{O}(\Delta x)$, and that the SG scheme has some advantages compared to the CN scheme.

5. Extension for nonlinear moisture transfer

The previous case study investigated the use of the numerical schemes for computing the solution of a linear problem of moisture convection. This second case study considers now nonlinear transfer, due to diffusion material properties depending on the moisture content $d_m^\star(u)$ and $c_m^\star(u)$. The PECLET number Pé is considered as constant, assuming

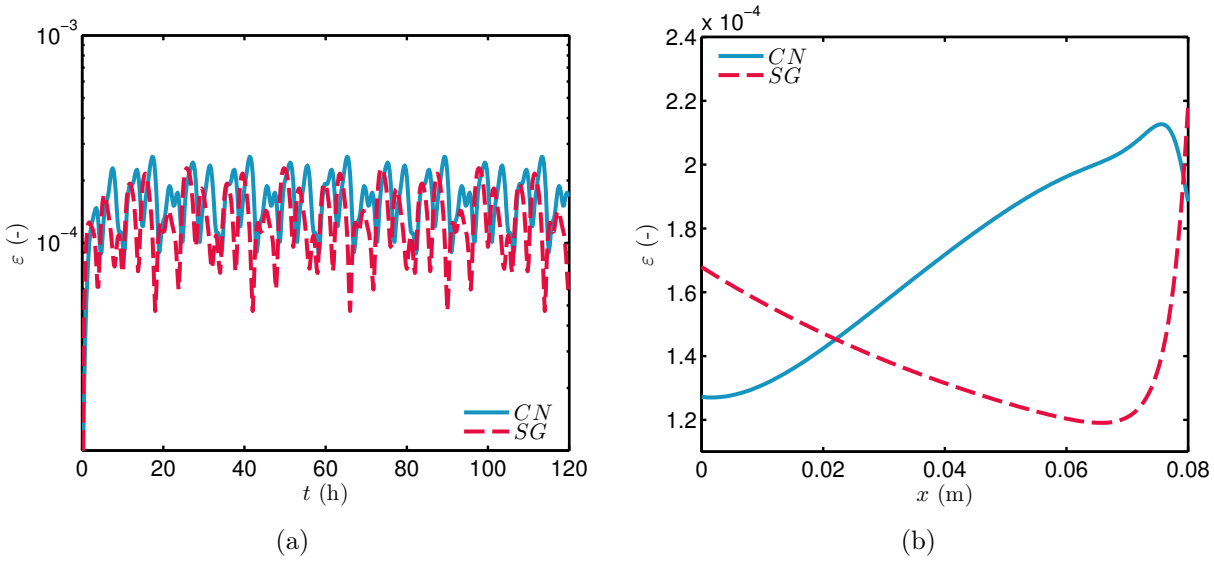

Figure 5. *L_2 error for fixed $\Delta x = 10^{-4}$ and $\Delta t = 10^{-3}$, in function of t (a) and in function of x (b).*

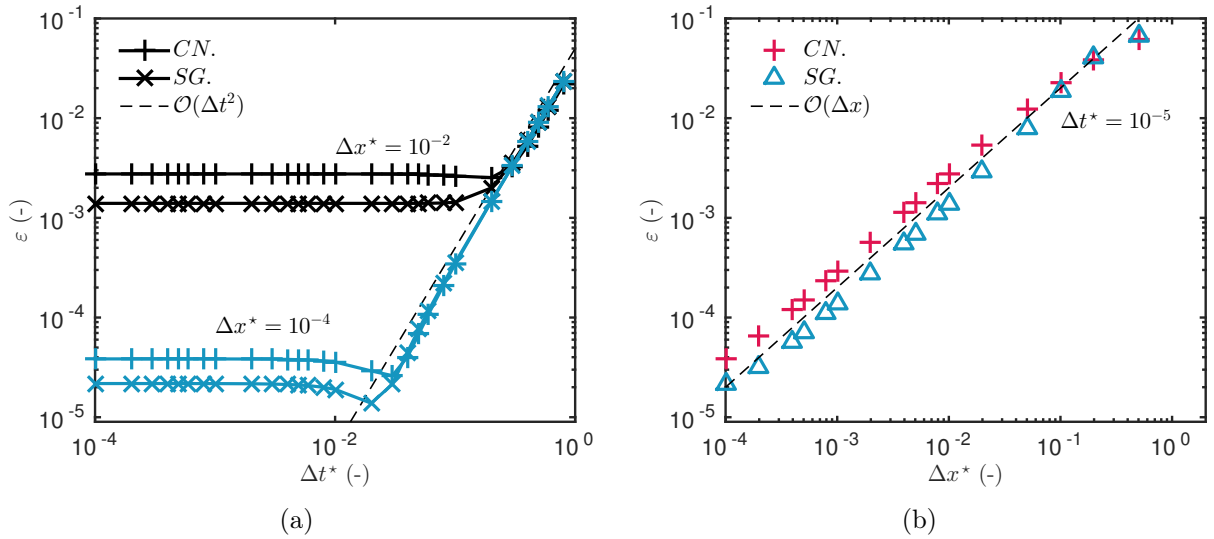

Figure 6. *L_2 error as a function of Δt for the CN and SG schemes ($\Delta x = 10^{-4}$) (a) and L_2 error as a function of Δx for the CN and SG schemes ($\Delta t = 10^{-5}$).*

a constant air velocity and temperature inside the material. In the next section, it will be considered as variable. This case will be investigated by means of the Scharfetter–Gummel and an improved version of the Crank–Nicolson schemes. First, the Crank–Nicolson and Scharfetter–Gummel schemes are detailed for the nonlinear case. For

this, Eq. (2.7) is re-called with a simplified notation:

$$c(u)\,\frac{\partial u}{\partial t} \;+\; \frac{\partial J}{\partial x} \;=\; 0\,, \qquad\qquad t \;>\; 0\,, \qquad\qquad x \;\in\; \left[0,\,1\right], \tag{5.1a}$$

$$J \;=\; \text{Pé}(u)\,u \;-\; d(u)\,\frac{\partial u}{\partial x}\,. \tag{5.1b}$$

5.1. The Crank–Nicolson scheme and its improved version

The straightforward application of the Crank–Nicolson scheme to Eq. (5.1a) yields the following scheme:

$$c_j^n\,\frac{u_j^{n+1} \;-\; u_j^n}{\Delta t} \;=\; \frac{1}{\Delta x}\left[J_{j+\frac{1}{2}}^{n+\frac{1}{2}} \;-\; J_{j-\frac{1}{2}}^{n+\frac{1}{2}}\right]. \tag{5.2}$$

Considering Eq. (3.3), we get:

$$\begin{aligned} J_{j+\frac{1}{2}}^{n+1} \;&=\; \left\{\begin{matrix} \text{Pé}_j^{n+1}\,u_j^{n+1}\,, & \text{Pé}_j^{n+1} \geqslant 0 \\ \text{Pé}_{j+1}^{n+1}\,u_{j+1}^{n+1}\,, & \text{Pé}_{j+1}^{n+1} < 0 \end{matrix}\right\} \;-\; \frac{1}{2}\,\left(d\,\frac{\partial u}{\partial x}\right)_{j+\frac{1}{2}}^{n+1} \\ &=\; \left\{\begin{matrix} \text{Pé}_j^{n+1}\,u_j^{n+1}\,, & \text{Pé}_j^{n+1} \geqslant 0 \\ \text{Pé}_{j+1}^{n+1}\,u_{j+1}^{n+1}\,, & \text{Pé}_{j+1}^{n+1} < 0 \end{matrix}\right\} \;-\; \frac{1}{2\,\Delta x}\,d_{j+\frac{1}{2}}^{n+1}\left(u_{j+1}^{n+1} \;-\; u_j^{n+1}\right). \end{aligned}$$

The numerical scheme is then written as:

$$\begin{aligned} &\left[1 \;+\; \gamma_{j+\frac{1}{2}}^{n+1}\,(\,\mathrm{b}^+ \;-\; \mathrm{b}^-\,) \;+\; \lambda_{j+\frac{1}{2}}^{n+1} \;+\; \lambda_{j-\frac{1}{2}}^{n+1}\right] u_j^{n+1} \\ &\qquad -\; \left[\lambda_{j+\frac{1}{2}}^{n+1} \;-\; \gamma_{j+\frac{1}{2}}^{n+1}\,\mathrm{b}^-\right] u_{j+1}^{n+1} \;-\; \left[\gamma_{j-\frac{1}{2}}^{n+1}\,\mathrm{b}^+ \;+\; \lambda_{j-\frac{1}{2}}^{n+1}\right] u_{j-1}^{n+1} \;= \\ &\qquad\qquad \left[1 \;-\; \gamma_{j+\frac{1}{2}}^{n}\,(\,\mathrm{b}^+ \;-\; \mathrm{b}^-\,) \;-\; \lambda_{j+\frac{1}{2}}^{n} \;+\; \lambda_{j-\frac{1}{2}}^{n}\right] u_j^n \;+ \\ &\qquad\qquad\qquad \left[\lambda_{j+\frac{1}{2}}^{n} \;-\; \gamma_{j+\frac{1}{2}}^{n}\,\mathrm{b}^-\right] u_{j+1}^n \;+\; \left[\gamma_{j-\frac{1}{2}}^{n}\,\mathrm{b}^+ \;+\; \lambda_{j-\frac{1}{2}}^{n}\right] u_{j-1}^n\,, \end{aligned}$$

where

$$\lambda_j \;=\; \frac{d_j\,\Delta t}{2\,\Delta x^2\,c_j}\,, \qquad \gamma_j \;=\; \frac{\text{Pé}_j\,\Delta t}{2\,\Delta x} \qquad \text{and} \qquad \mathrm{b}^{\pm} \;=\; \frac{1 \pm \mathrm{sign}(\text{Pé})}{2}\,.$$

However, this approach leads to deal with nonlinearities associated to the quantities of the flux (as $d_{j+\frac{1}{2}}^{n+1}$ and Pé_j^{n+1}) at the upcoming time layer $t \;=\; t^{n+1}$. To deal with this issue, linearisation techniques as Picard or Newton–Raphson ones [7, 40], can be employed but requiring a high number of sub-iterations.

To overcome these difficulties, it is possible to evaluate the diffusion coefficient at the current time layer instead of the upcoming one [1]. Thus, the convection flux at the

interface becomes:

$$J^{n+1}_{j+\frac{1}{2}} = \left\{ \begin{array}{ll} \text{Pé}^n_j \; u^{n+1}_j \,, & \text{Pé}^n_j \geqslant 0 \\ \text{Pé}^n_j \; u^{n+1}_{j+1} \,, & \text{Pé}^n_j < 0 \end{array} \right\} - \frac{1}{2\,\Delta x} \, d^n_{j+\frac{1}{2}} \left(u^{n+1}_{j+1} - u^{n+1}_j \right).$$

Finally, the modified Crank–Nicolson schemes yields to:

$$\begin{aligned} \left[1 + \gamma^n_{j+\frac{1}{2}} \, (\mathrm{b}^+ - \mathrm{b}^-) + \lambda^n_{j+\frac{1}{2}} + \lambda^n_{j-\frac{1}{2}} \right] u^{n+1}_j \\ - \left[\lambda^n_{j+\frac{1}{2}} - \gamma^n_{j+\frac{1}{2}} \, \mathrm{b}^- \right] u^{n+1}_{j+1} - \left[\gamma^n_{j-\frac{1}{2}} \, \mathrm{b}^+ + \lambda^n_{j-\frac{1}{2}} \right] u^{n+1}_{j-1} = \\ \left[1 - \gamma^n_{j+\frac{1}{2}} \, (\mathrm{b}^+ - \mathrm{b}^-) - \lambda^n_{j+\frac{1}{2}} + \lambda^n_{j-\frac{1}{2}} \right] u^n_j + \\ \left[\lambda^n_{j+\frac{1}{2}} - \gamma^n_{j+\frac{1}{2}} \, \mathrm{b}^- \right] u^n_{j+1} + \left[\gamma^n_{j-\frac{1}{2}} \, \mathrm{b}^+ + \lambda^n_{j-\frac{1}{2}} \right] u^n_{j-1}, \end{aligned} \tag{5.3}$$

The combination of IMplicit-EXplicit (*IMEX*) approaches clearly appear in this formulation of Eq. (5.3). The major advantage over the classical Crank–Nicolson scheme is to avoid sub-iterations in the solution procedure, without loosing the accuracy and the stability.

5.2. The Scharfetter–Gummel scheme

In the nonlinear case, the Scharfetter–Gummel numerical schemes is written as:

$$c^n_j \, \frac{u^{n+1}_j - u^n_j}{\Delta t} = \frac{1}{\Delta x} \left[J^{n+\frac{1}{2}}_{j+\frac{1}{2}} - J^{n+\frac{1}{2}}_{j-\frac{1}{2}} \right]. \tag{5.4}$$

We use the hypothesis of frozen coefficient on the interval $\left[x^n_j, \, x^n_{j+1} \right]$. Thus, the flux at each interface $x_{æ+\frac{1}{2}}$ is computed with following boundary value problem:

$$J^n_{j+\frac{1}{2}} = \text{Pé}^n_{j+\frac{1}{2}} \, u - d^n_{j+\frac{1}{2}} \, \frac{\partial u}{\partial x}, \qquad \forall x \in \left[x^n_j, \, x^n_{j+1} \right], \tag{5.5a}$$

$$u = u^n_j, \qquad x = x^n_j, \tag{5.5b}$$

$$u = u^n_{j+1}, \qquad x = x^{n+1}_j. \tag{5.5c}$$

The solution of Eq. (5.5) is:

$$J^n_{j+\frac{1}{2}} = \frac{1}{\Delta x} \, d^n_{j+\frac{1}{2}} \left[- \mathcal{B}\left(\frac{\Delta x}{d^n_{j+\frac{1}{2}}} \, \text{Pé}^n_{j+\frac{1}{2}} \right) u^{n+1}_j + \mathcal{B}\left(- \frac{\Delta x}{d^n_{j+\frac{1}{2}}} \, \text{Pé}^n_{j+\frac{1}{2}} \right) u^n_j \right].$$

When dealing with the nonlinearities of the material properties, an interesting feature of explicit schemes is that it does not require any sub-iterations (using Newton–Raphson

approach for instance). At the time iteration n, the material properties c_j, $d_{j+\frac{1}{2}}$, $d_{j-\frac{1}{2}}$ are *explicitly* calculated at t^n. The CFL condition of the scheme is given by Gosse [15]:

$$\Delta t \cdot \max_{x\in[0,1]} \left[\frac{\text{Pé}}{d^\star_m} \tanh\left(\frac{\text{Pé}\,\Delta x}{2\,d^\star_m} \right)^{-1} \right] \leqslant \Delta x \cdot \frac{c^\star_m}{d^\star_m}\,. \tag{5.6}$$

5.3. Numerical application

The dimensionless properties of the materials are:

$$d^\star_m = 1 + 0.91\,u + 600 \cdot \exp\left[-10\left(u - 2.3 \right)^2 \right],$$
$$c^\star_m = 900 - 400\,u + 10^4 \cdot \exp\left[-10\left(u - 2.3 \right)^2 \right].$$

From a physical point of view, the storage and diffusion coefficients are given in Figures 7(a) and 7(b). Their variations with the relative humidity are similar to the load bearing material from [20]. The PÉCLET number is equal to Pé $=$ 10 corresponding to an air velocity of 0.01 $\mathsf{m/s}$. A first order approximation of the air transfer in porous material is given by [4]:

$$\mathsf{v} = -\frac{\kappa_m}{\mu_a}\frac{\partial P}{\partial x}\,, \tag{5.7}$$

where κ_m is the air permeability of the material, $\mu_a = 1.8 \cdot 10^{-5}$ $\mathsf{Pa.s}$ is the dynamic viscosity of air and P is the air pressure. Therefore, such condition can be obtained for a material with an air permeability of the order of $\kappa_m = 10^{-9}$ m^2, with an air pressure difference, between both sides of the material, of 10 Pa. These conditions easily occur in buildings. Moreover, a number of hygroscopic building materials as cellulose, wood fibre or hemp concrete, has an air permeability of such order [2, 23].

The initial vapour pressure is uniform $P^i_v = 1.16 \cdot 10^3$ Pa, corresponding to a relative humidity $\varphi = 50$ %. No liquid flow is taken into account at the boundaries. The BIOT numbers are fixed to $\text{Bi}^{\text{L}}_v = 28.75$ and $\text{Bi}^{\text{R}}_v = 4.28$. The ambient vapour pressure at the boundaries are different from the previous case study, u^{R} and u^{L} follow sinusoidal variations from the dry to saturate state, forcing periodical conditions:

$$u^{\text{R}} = 1 + 0.85\,\sin\left(\frac{2\pi}{24}\,t^\star \right) + 0.1\,\sin\left(4\pi\,t^\star \right),$$
$$u^{\text{L}} = 1 + 0.5\,\sin\left(\frac{2\pi}{12}\,t^\star \right).$$

The physical boundary conditions are illustrated in Figure 8. The material is thus excited until the capillary state. The final simulation time is fixed to $\tau^\star = 48$.

The solution of the problem has been computed with following discretisation parameters: $\Delta t^\star = 1 \cdot 10^{-3}$ and $\Delta x^\star = 1 \cdot 10^{-2}$. The time variation of the vapour pressure on the two extremities of the building component is given in Figure 9(a). The vapour pressure

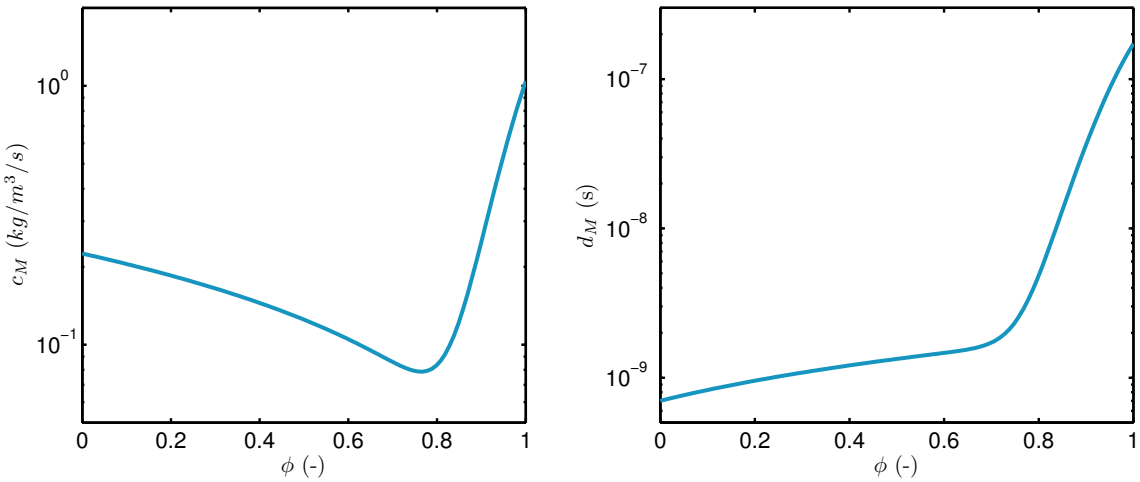

Figure 7. *Variation of the moisture storage c_M (a) and diffusion d_M (b) as a function of the relative humidity ϕ.*

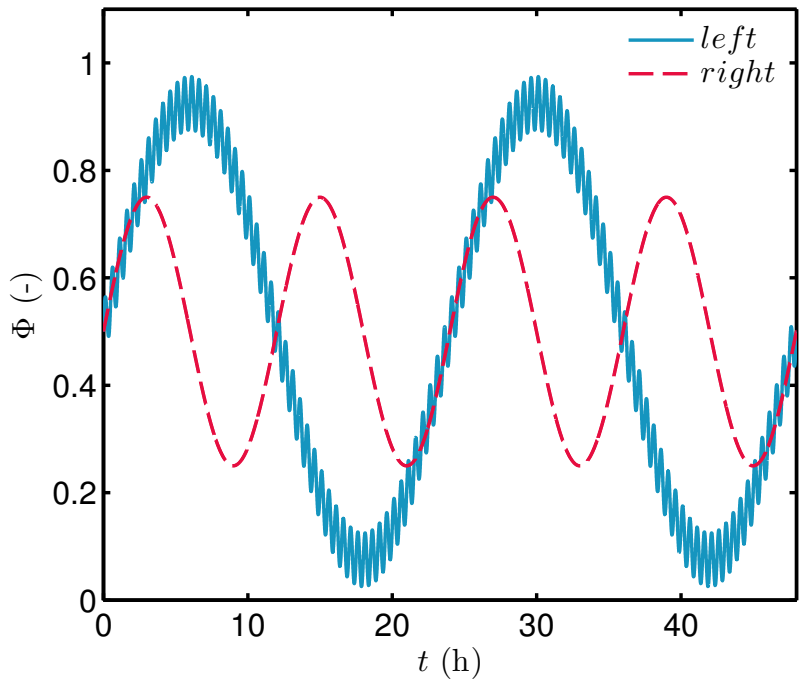

Figure 8. *Boundary conditions.*

is increasing according to the variation at the left boundary condition, which has a higher BIOT number and a higher amplitude. The diffusion process can be observed going from the left to the right boundary. The diffusion process can also be seen on the three profiles of the vapour pressure illustrated in Figure 9(b).

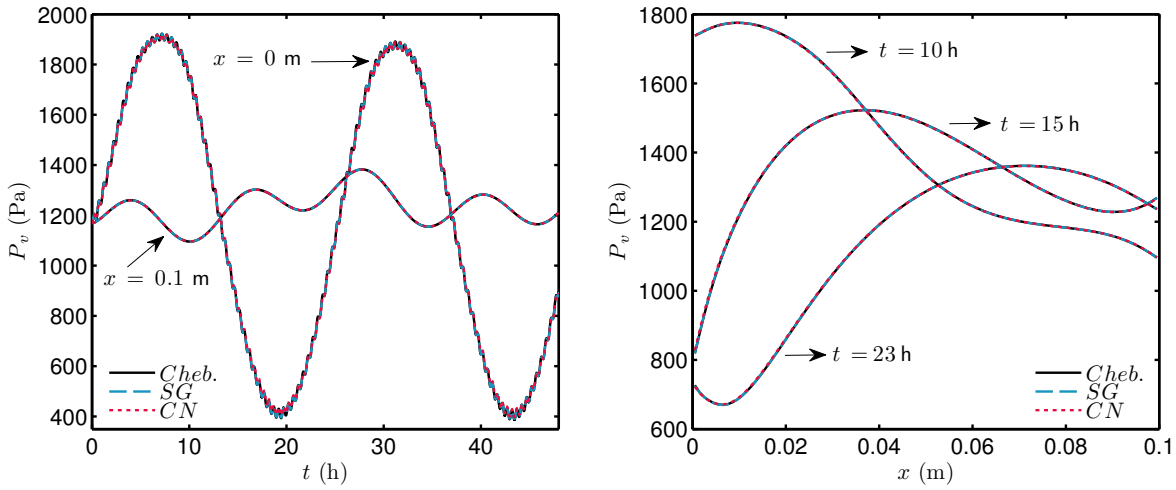

(a) (b)

Figure 9. *Vapour pressure time evolution at* $x \in \{0, 0.1\}$ m *(a) and profiles for* $t \in \{10, 15, 23\}$ h *(b).*

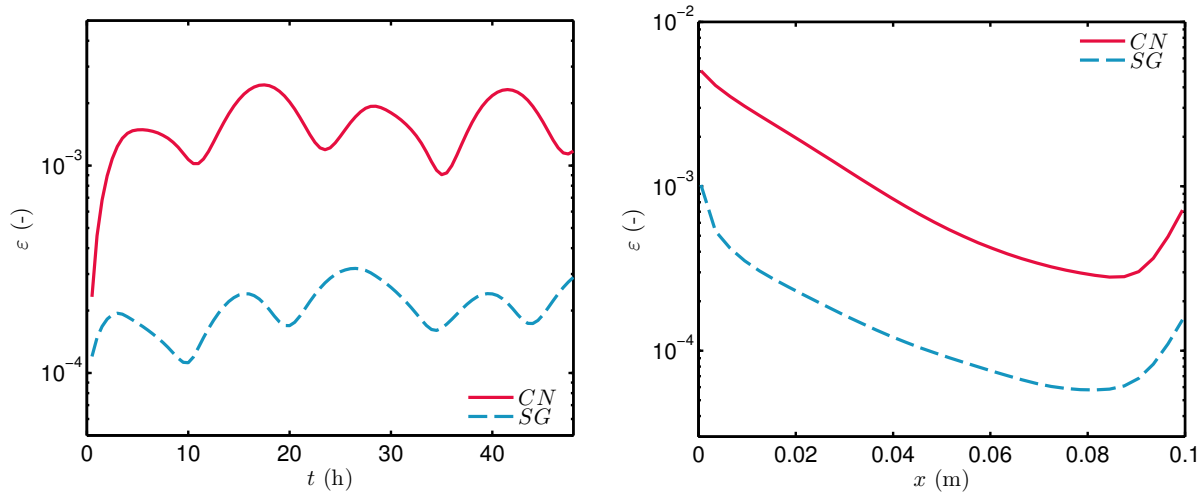

(a) (b)

Figure 10. L_2 *error as a function of time* t *(a) and as a function of space* x *(b).*

Both schemes succeed in representing the advection-diffusion phenomena in the building component. The L_2 error of the Crank–Nicolson and of the Scharfetter–Gummel schemes are presented in Figure 10(a) and in Figure 10(b), one in function of time and the other in function of the space. The Scharfetter–Gummel scheme has shown to be more accurate than the Crank–Nicolson one. For a better understanding of the accuracy of the schemes a convergence study is presented.

The problem is then computed with $\Delta x^\star = 10^{-2}$ and for different values of $\Delta t^\star$. For each value of $\Delta t^\star$, the L_2 error was computed between the solutions of the schemes and a

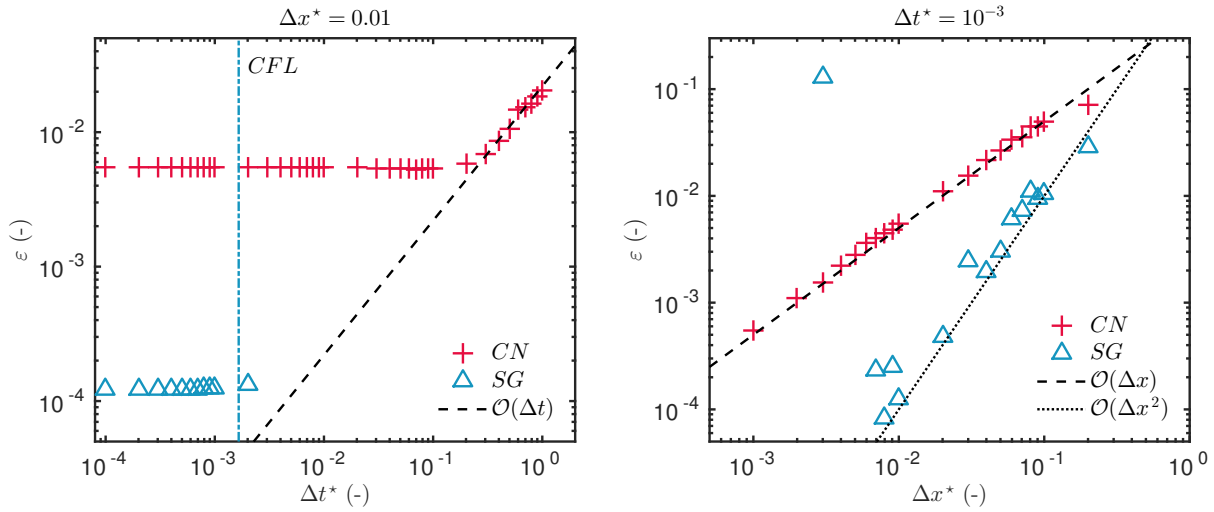

Figure 11. *L_2 error ε for a fixed $\Delta x^\star = 10^{-2}$ as a function of $\Delta t^\star$ (a), and L_2 error ε for a fixed $\Delta t^\star = 10^{-3}$ as a function of $\Delta x^\star$.*

Chebfun reference solution. Figure 11(a) shows the results of this convergence study. Meanwhile in Figure 11(b) the $\Delta t^\star$ is fixed to 10^{-3} and the L_2 error is computed for different values of $\Delta x^\star$. The CFL condition of the Scharfetter–Gummel scheme is given by Eq. (5.6), with $\Delta t^\star \leqslant 1 \cdot 10^{-3}$. The Scharfetter–Gummel scheme can only be computed when the CFL condition is respected, while the modified Crank–Nicolson scheme is unconditionally stable (at least for linear problems). Despite of the stability of the modified Crank–Nicolson scheme, the Scharfetter–Gummel approach gains in terms of accuracy. Moreover, the stability of the modified Crank–Nicolson scheme does not neccessary imply an accurate solution [36]. The choice of the discretisation depends on the boundary condition as well as the characteristic diffusion time in the material, to accurately represent the physical phenomenon. Figure 11(a) reveals that the modified Crank–Nicolson is first order of accuracy in time $\mathcal{O}(\Delta t)$. The modification of the classical Crank–Nicolson scheme implies loosing the $\mathcal{O}(\Delta t^2)$ accuracy in an effort to avoid the sub-iterations due to nonlinearities. For the Scharfetter–Gummel scheme, it is not possible to verify the order of accuracy in time. Indeed, before the CFL condition, the error of the scheme is influenced by the order of $\Delta x^\star$. In Figure 11(b) the order of accuracy regarding the space discretisation, corresponds to $\mathcal{O}(\Delta x^2)$ for Scharfetter–Gummel and $\mathcal{O}(\Delta x)$ for the modified Crank–Nicolson. Besides the CFL condition, the Scharfetter–Gummel scheme has a minimum restriction regarding to $\Delta x^\star$. If the value of $\Delta x^\star$ is below the limit, the solution diverges.

An interesting advantage of the Scharfetter–Gummel scheme compared to the Crank–Nicolson approach, is the ease of implementation. The algorithm is written using an explicit formulation and the fluxes are calculated analytically for each mesh element. It may allow to achieve almost perfect scaling on high-performance computer systems [8].

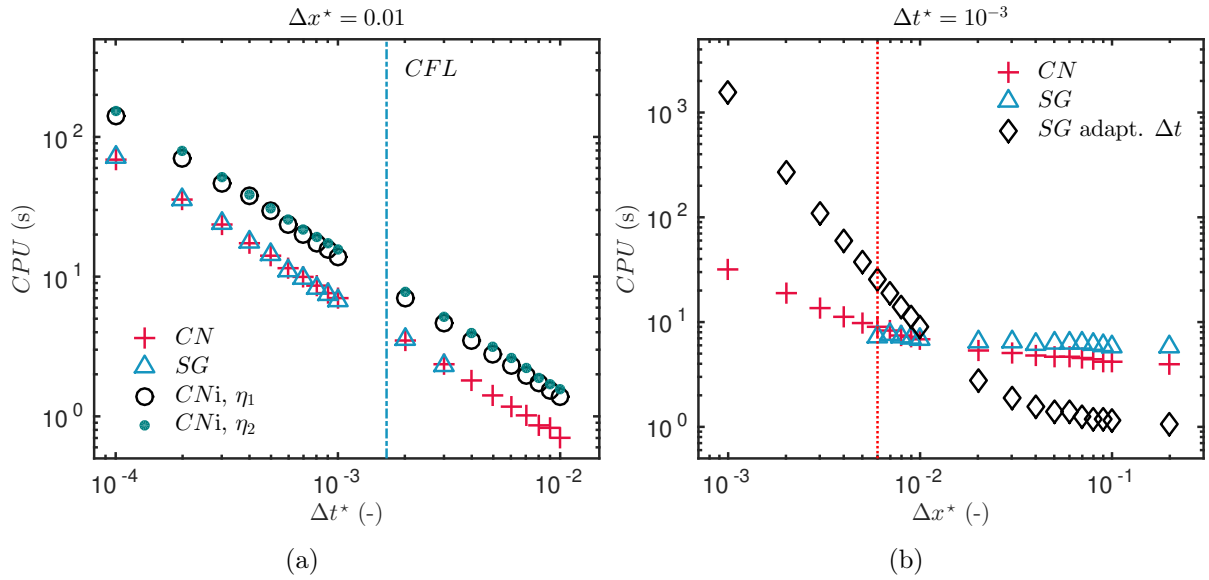

Figure 12. *Computational time for* $\Delta x = 10^{-2}$ *as a function of* Δt *(a), and for* $\Delta t = 10^{-3}$ *as a function of* Δx *.*

For this numerical application, the CPU time of each numerical scheme has been evaluated using `Matlab` platform on a computer using Intel i7 CPU and 32GB of RAM. Results are presented in Figure 12(a) as a function of Δx and in Figure 12(b) as function of Δt. The Crank–Nicolson and Scharfetter–Gummel schemes have the same order of magnitude of CPU time. On the other hand, the Scharfetter–Gummel scheme has been implemented with an adaptive Δt using `Matlab` function `ode113`. As illustrated in Figure 12(b), it enables to gain a significant computational time when Δx is relatively large, whithout loosing any accuracy. The classical Crank–Nicolson scheme has also been used to compute a problem solution, using a tolerance $\eta_1 = \Delta t$ and $\eta_2 = 0.5\,\Delta t$ for the convergence of the sub-iterations required to treat the nonlinearities. Figure 12(a) shows that the CPU time is almost multiplied by two using this approach. Thus, the use of the classical Crank–Nicolson scheme has strong disadvantages compared to the two other proposed schemes. The modified Crank–Nicolson and Scharfetter–Gummel approaches enable to compute an accurate solution two times faster.

Table 1 summarises the features of both numerical schemes investigated, highlighting the efficiency of the Scharfetter–Gummel approach to solve the advective-diffusive moisture equation.

6. Comparing numerical results with experimental data

Previous sections aimed at illustrating the advantages of the Scharfetter–Gummel scheme to compute the problem of moisture transfer by diffusion and advection mechanisms

Scharfetter–Gummel
• Well balanced
• Asymptotic preserving
• Explicit form of the solution, no sub-iterations required to treat the non-linearities
• CFL stability condition scaling with Δx for large spatial grid
• Reduced CPU with an adaptive time step algorithm
• Lower absolute accuracy
modified Crank–Nicolson
• Unconditionally stable (at least for linear problems)
• Explicit expression of the material properties, no sub-iterations required to treat the non-linearities

Table 1. *Synthesis of the numerical schemes features.*

through a porous material, which can be used to reduce the discrepancies between experimental and numerical results. For this, experimental data from [19] are used for the comparison, which considered a gypsum board initially conditioned at $\varphi = 0.3$, submitted to a 48 h adsorption-desorption cycle (30–72–30). A constant surface transfer coefficient is assumed equal to $2.41 \cdot 10^{-8}$ $\mathsf{s/m}$ and the material properties are given in Table 2 from [19].

The Scharfetter–Gummel numerical scheme has been used to compute the solution of the moisture transfer in the material, considering $\Delta x^\star = 10^{-2}$ and an adaptive time step. It should be noted that the Crank–Nicolson approach could have been used to compute the solution. It would also provide an accurate solution to analyse the physical phenomena. Nevertheless, given all the advantages reported in Table 1, the Scharfetter–Gummel scheme was choosen for this comparison. Figures 13(a) and 13(b) show the evolution of the relative humidity computed with a constant Péclet number and with a model considering only moisture diffusion. The Péclet number has been estimated as $\mathrm{Pé} = 1.8$, ensuring a $\mathcal{L}_2$ error with measurement $\varepsilon = 5 \cdot 10^3$. The moisture diffusion model provides the same trends as the results from [19] but does not represent well the physical phenomenon since it ignores the important advective contribution to the moisture transfer. The numerical results from the convection model do not underestimate the adsorption process or overestimate the desorption process, contrarily to the model that only considers the diffusion as a transport mechanism.

Remembering that $\mathrm{Pé} = \dfrac{\mathsf{v} \cdot L}{R_v \cdot T \cdot d_m^0}$, the Péclet number has been estimated as $\mathrm{Pé} = 1.8$. We assume the temperature in the material is 23 $\mathsf{°C}$, the reference moisture transport coefficient is $d_m^\star = 7.3 \cdot 10^{-10}$ s and the length of the material is $L = 37.5$ mm. The air velocity in the material is then $\mathsf{v} = 5 \cdot 10^{-3}$ $\mathsf{m/s}$. On the other hand,

the air velocity in the material is given by Eq. (5.7) where $\kappa_m = 4 \cdot 10^{-9}$ m^2 is the air permeability of the material [23]. Thus, at the point of observation $x = 12.5$ mm, the estimated air velocity is due to a difference of air pressure of $\Delta P = 3$ Pa, which is reasonable considering the experimental set-up.

In order to compare the relative importance of the terms of advective-diffusive moisture governing equation (Eq. (2.1)), a brief and local sensitivity analysis is carried out by defining the following sensitivity functions Θ:

$$\Theta_d = d_m^\star \frac{\partial \varphi}{\partial d_m^\star}, \qquad \Theta_{\text{Pé}} = \text{Pé} \frac{\partial \varphi}{\partial \text{Pé}}.$$

Each sensitivity function Θ evaluates the sensitivity of the numerically computed field φ with respect to parameter $d_m^\star$ and Pé. A small magnitude value of Θ indicates large changes in the parameter yield small changes in φ. Figures 14(a) and 14(b) provides the time evolution of the sensitivity Θ for each parameter, at both measurement points. The sensitivity increases at the moment corresponding to the transient regimes of the simulation ($t \in [0,\ 10] \cup [24,\ 34]$ h). Then, it decreases as the simulation reach the steady state regime. At $x = 12.5$ mm, the relative humidity is more sensible to $d_m^\star$ than Pé. At $x = 25$ mm, both parameters have the same order of magnitude of sensitivity. This local sensitivity analysis illustrates the importance of considering the moisture advection transfer for this material and for the relative humidity range used in the experiments from [19].

The PÉCLET number varies as a function of the inverse of the temperature. In Section 2, it was assumed the variation of temperature in the material as negligible. Here, this assumption is disconsidered as the experimental data from [19] also provides the temperature evolution in the material, as shown in Figure 15(a) represented as $\frac{1}{T}$. Five different periods can be observed, corresponding to increase or decrease steps. To improve the results, the PÉCLET number has been estimated as a function of time and according to those five different periods. This estimation yields to a L_2 error of $\varepsilon = 1.1 \cdot 10^3$. Figure 15(b) illustrates the time evolution of Pé at the two measurement points. As it can be noticed in Figures 13(a) and 13(b), with the correction on PÉCLET number, the numerical results fit better with the experimental data. These results highlight that Pé also varies with x, probably due to the variation of the air pressure (and therefore the air velocity) in the material.

7. Conclusions

Numerous studies in the literature reported slower transient behaviour of moisture evolution, obtained by numerical models that consider only moisture diffusion through porous materials, when compared to experimental data. Although, the discrepancies might come from different reasons such as hysteresis, uncertainties on moisture storage and transport coefficients, and material anisotropy, the results presented in this paper reveals that the advective moisture transfer may play an important role on providing much more accurate

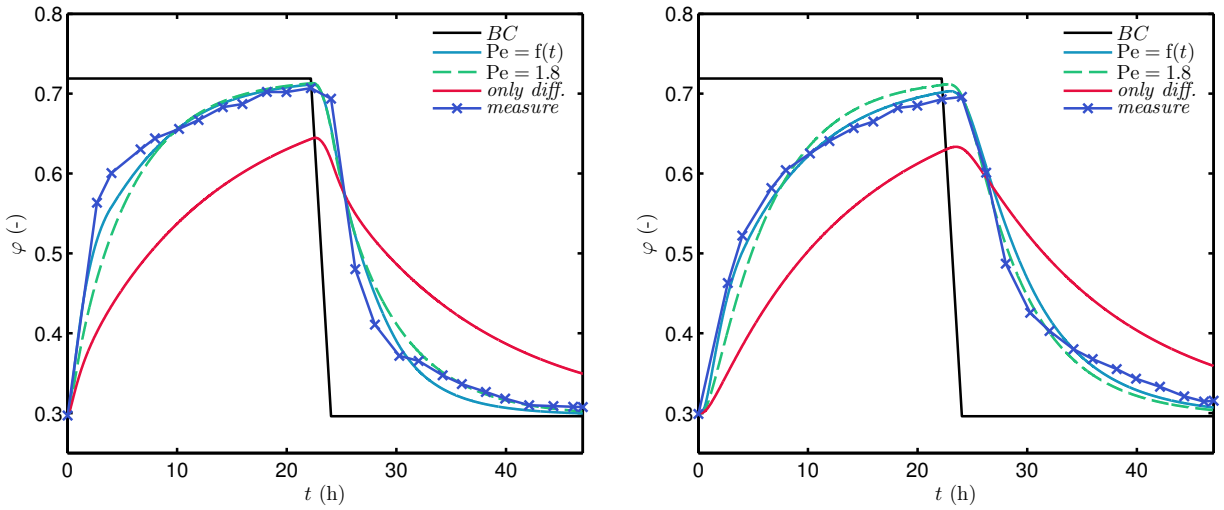

Figure 13. *Measured and simulated relative humidity at* $x = 12.5$ mm *(a) and* $x = 25$ mm *(b).*

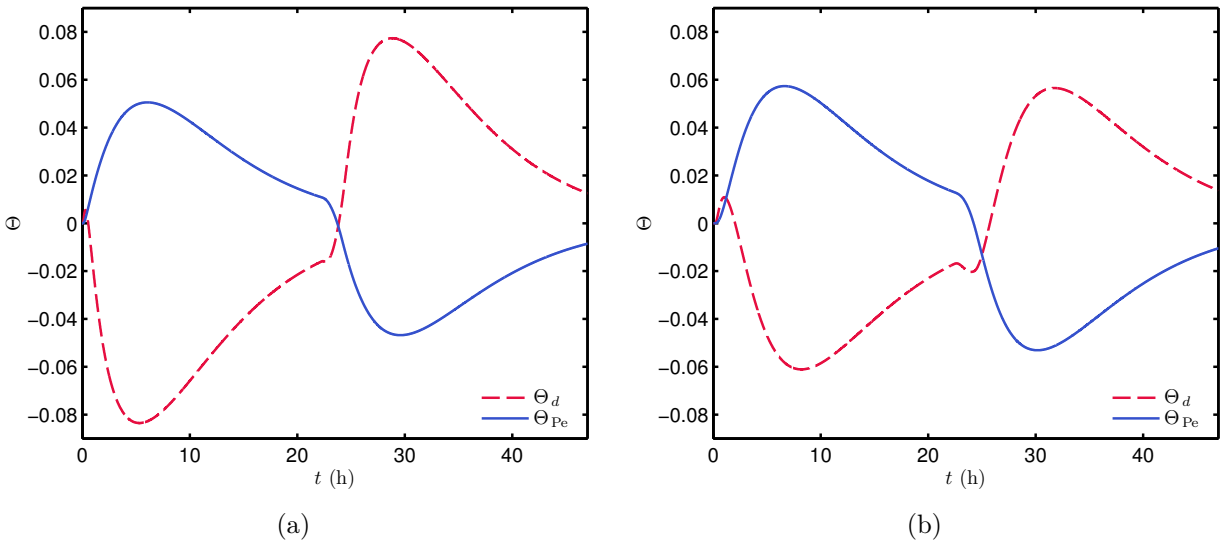

Figure 14. *Sensitivity coefficients of parameters* $c_m^\star$, $d_m^\star$ *and* P*é at* $x = 12.5$ mm *(a) and* $x = 25$ mm *(b).*

results for relative humidity range within 30-70% and for materials with a microstructure composed of larger pores. To solve the advective-diffusive problem, two numerical schemes have been proposed and their efficiencies have been compared for both linear and non-linear cases. The Scharfetter–Gummelscheme has been compared to the extensively used Crank–Nicolson approach. The Scharfetter–Gummel scheme is based on an implicit-explicit discretisation of the equations. It has been proposed in 1969 , based on

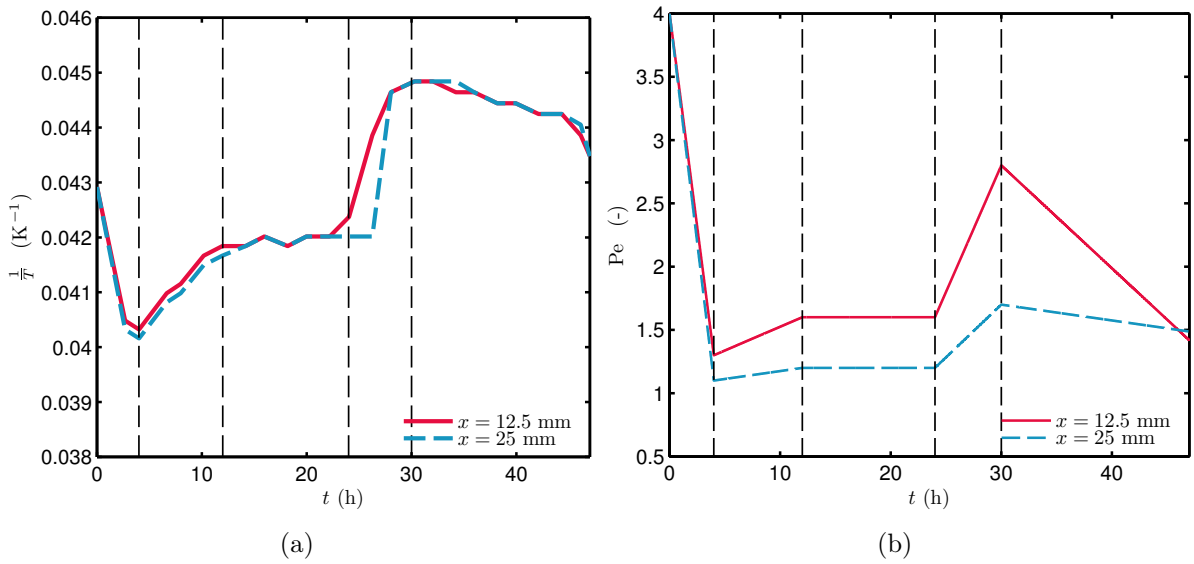

Figure 15. *Time evolution of* $\frac{1}{T}$ *(a) and the estimated* PÉCLET *number (b).*

the solution of the POINCARÉ–STEKLOV operator to compute an analytical expression of the diffusion and advection fluxes at each mesh interface. Performance of both schemes were analysed for the two case studies.

The first case study considered a linear convective transfer through a porous material. The schemes solution were compared to a reference solution obtained using CHEBYSHEV functions. Results have shown that both are first-order accurate in space $\mathcal{O}(\Delta x)$ and second-order in time $\mathcal{O}(\Delta t)^2$. The solution computed with SCHARFETTER–GUMMEL scheme is more accurate. The second case study focused on nonlinear transfer, with material properties dependent on the vapour pressure field. The extension of the CRANK–NICOLSON and SCHARFETTER–GUMMEL schemes were given specially to treat the nonlinearities of the problem. A modified CRANK–NICOLSON was proposed in order to avoid sub-iterations at each time step of the algorithm. Both modified CRANK–NICOLSON and SCHARFETTER–GUMMEL schemes were used to compute the solution of the problem with accuracy. Results have shown that the error is proportional to $\mathcal{O}(\Delta t)$. The SCHARFETTER–GUMMEL scheme has a CFL restriction stability but is more accurate than the modified CRANK–NICOLSON approach. Moreover, the stability of the CRANK–NICOLSON scheme does not neccessary imply an accurate solution [36]. The choice of the time discretisation Δt is an important issue to represent accurately the physical phenomenon. Both schemes have the same order of CPU time. The classical CRANK–NICOLSON approach has shown to be twice as slow. Furthermore, the CPU time of the SCHARFETTER–GUMMEL scheme can be reduced using an adaptive time step Δt, thanks to the CFL stability condition scaling with Δx when considering large spatial discretisation.

In the last section, the SCHARFETTER–GUMMEL scheme was used to compute the solution of a moisture convective problem from the literature with experimental data provided

from [19]. The purpose was to highlight the impact of the advection on the moisture transfer. The moisture diffusion model reveals the slower transient behaviour whereas the results of the convective moisture model shows good agreement with the experimental data. The PÉCLET number, quantifying the advection transfer, has been estimated. A local sensitivity analysis has shown the importance of the PÉCLET number in the numerical model. The dependency of the PÉCLET number to temperature has also been highlighted. Thus, further work should be focused on models combining heat, air and moisture transfer considering both diffusion and advection terms and using the SCHARFETTER–GUMMEL numerical scheme for a fast computation of an accurate solution. The importance of the advective term should also be further investigated and compared to the capacitive and diffusive terms, considering hysteresis, for both pendular and funicular states.

Acknowledgements

The authors acknowledge the Brazilian Agencies CAPES of the Ministry of Education, the CNPQ of the Ministry of Science, Technology and Innovation, for the financial support. The authors also would like to acknowledge Dr. L. Gosse (IAC–CNR "Mauro Picone", Italy) for his precious discussions on numerical matters.

Nomenclature

	Latin letters	
d_m	moisture diffusion	[s]
c_m	moisture storage capacity	[kg/m^3/Pa]
g	liquid flux	[kg/m^2/s]
h_v	vapour convective transfer coefficient	[s/m]
k	permeability	[s]
L	length	[m]
P_c	capillary pressure	[Pa]
P_s	saturation pressure	[Pa]
P_v	vapour pressure	[Pa]
R_v	water gas constant	[J/kg/K]
T	temperature	[K]
v	air velocity	[m/s]
	Greek letters	
ϕ	relative humidity	[−]
ρ	specific mass	[kg/m^3]
κ	air permeability	[m^2]
μ	dynamic viscosity	[Pa.s]
	Dimensionless parameters	
a	advection coefficient	[−]
Bi	BIOT number	[−]
$c_m^\star$	storage coefficient	[−]
$d_m^\star$	permeability coefficient	[−]
J	flux	[−]
$g^\star$	liquid flow	[−]
Pé	PECLET number	[−]
u	field	[−]
ν	diffusion coefficient	[−]

References

[1] U. M. Ascher, S. J. Ruuth, and B. T. R. Wetton. Implicit-Explicit methods for time-dependent partial differential equations. *SIAM J. Numer. Anal.*, 32(3):797–823, 1995. 17

[2] ASHRAE. Chapter 26: Heat, Air, and Moisture Control in Building Assemblies - Material Properties. In *ASHRAE Handbook - Fundamentals*, page 1000. American Society of Heating, Refrigerating and Air-Conditioning Engineers, Inc., 2013. 19

[3] B. Bauklimatik Dresden. Simulation program for the calculation of coupled heat, moisture, air, pollutant, and salt transport. *http://www.bauklimatik-dresden.de/delphin/index.php?aLa=en*, 2011. 4

[4] C. Belleudy, M. Woloszyn, M. Chhay, and M. Cosnier. A 2D model for coupled heat, air, and moisture transfer through porous media in contact with air channels. *Int. J. Heat Mass Transfer*, 95:453–465, apr 2016. 5, 6, 19

[5] J. Berger, S. Guernouti, M. Woloszyn, and C. Buhe. Factors governing the development of moisture disorders for integration into building performance simulation. *J. Building Eng.*, 3:1–15, sep 2015. 4

[6] D. M. Burch. An Analysis of Moisture Accumulation in Walls Subjected to Hot and Humid Climates. *ASHRAE Transactions*, 93(16):429–439, 1993. 4

[7] E. Cajori. Historical note on the Newton-Raphson method ofapproximation. *Amer. Math.*, 18:29–32, 1911. 17

[8] B. N. Chetverushkin and A. V. Gulin. Explicit schemes and numerical simulation using ultrahigh-performance computer systems. *Doklady Mathematics*, 86(2):681–683, sep 2012. 22

[9] T. Colinart, D. Lelievre, and P. Glouannec. Experimental and numerical analysis of the transient hygrothermal behavior of multilayered hemp concrete wall. *Energy and Buildings*, 112:1–11, jan 2016. 4, 5

[10] J. Crank, P. Nicolson, and D. R. Hartree. A practical method for numerical evaluation of solutions of partial differential equations of the heat-conduction type. *Mathematical Proceedings of the Cambridge Philosophical Society*, 43:50–67, jan 1947. 9

[11] T. A. Driscoll, N. Hale, and L. N. Trefethen. Chebfun Guide. *Pafnuty Publications*, Oxford, 2014. 13, 15

[12] A. Fabbri, F. Sallet, H. K. K. Wong, and J. C. Morel. Hygrothermal behaviour of hemp concrete: experimental evidences and modelling. In *VI International Conference on Computational Methods for Coupled Problems in Science and Engineering*, 2015. 4

[13] I. Fraunhofer. Wufi. *http://www.hoki.ibp.fhg.de/wufi/wufi_frame_ e.html*, 2005. 4

[14] L. Gosse. *Computing Qualitatively Correct Approximations of Balance Laws: Exponential-Fit, Well-Balanced and Asymptotic-Preserving*, volume 2 of *SIMAI Springer Series*. Springer Milan, Milano, 1 edition, 2013. 11, 12

[15] L. Gosse. L-splines and viscosity limits for well-balanced schemes acting on linear parabolic equations. *Preprint*, Submitted:1–21, 2016. 13, 19

[16] L. Gosse. Viscous equations treated with L-splines and Steklov-Poincare operator in two dimensions. In L. Gosse and R. Natalini, editors, *Innovative Algorithms and Analysis*. Springer International Publishing, Milano, 2017. 11, 12

[17] E. Hairer, S. P. Nørsett, and G. Wanner. *Solving ordinary differential equations: Nonstiff problems*. Springer, 2009. 9

[18] S. Y. Harris. *Building Pathology: Deterioration, Diagnostics, and Intervention*. Wiley, New York, 2001. 4

[19] C. James, C. J. Simonson, P. Talukdar, and S. Roels. Numerical and experimental data set for benchmarking hygroscopic buffering models. *Int. J. Heat Mass Transfer*, 53(19-20):3638–3654, sep 2010. 4, 5, 24, 25, 28

[20] H. Janssen. Simulation efficiency and accuracy of different moisture transfer potentials. *Journal of Building Performance Simulation*, 7(5):379–389, sep 2014. 6, 19

[21] J. W. Jerome. Drift-Diffusion Systems: Variational Principles and Fixed Point Maps for Steady State Semiconductor Models. In *Computational Electronics*, pages 15–20. Springer US, Boston, MA, 1991. 12

[22] W. Kahan and J. Palmer. On a proposed floating-point standard. *ACM SIGNUM Newsletter*, 14(si-2):13–21, oct 1979. 8

[23] M. Kumar Kumaran. *International Energy Agency energy conservation in buildings and community systems programme Heat, air and moisture transfer through new and retrofitted insulated envelope parts: [IEA] (Hamtie); Annex 24 Task 3/Final report: Material properties*. Laboratorium Bouwfysica, Dep. Burgerlijke Bouwkunde, K.U.-Leuven, Leuven, Belgium, 1996. 5, 19, 25

[24] H. M. Kunzel and J. Kiessl. *Simultaneous heat and moisture transport in building components: one- and two-dimensional calculation using simple parameters*. IRB Verlag, 1995. 4

[25] J. Kwiatkowski, M. Woloszyn, and J.-J. Roux. Modelling of hysteresis influence on mass transfer in building materials. *Building and Environment*, 44(3):633–642, mar 2009. 5

[26] M. Labat, M. Woloszyn, G. Garnier, and J. J. Roux. Dynamic coupling between vapour and heat transfer in wall assemblies: Analysis of measurements achieved under real climate. *Building and Environment*, 87:129–141, may 2015. 5

[27] D. Lelievre, T. Colinart, and P. Glouannec. Hygrothermal behavior of bio-based building materials including hysteresis effects: Experimental and numerical analyses. *Energy and Buildings*, 84:617–627, dec 2014. 4, 5

[28] R. J. Liesen. *Development of a Response Factor Approach for Modeling the Energy Effects of Combined Heat and Mass Transfer with Vapor Adsorption in Building Elements*. Phd, University of Illinois, 1994. 4

[29] C. Maalouf, A. T. Le, S. B. Umurigirwa, M. Lachi, and O. Douzane. Study of hygrothermal behaviour of a hemp concrete building envelope under summer conditions in France. *Energy and Buildings*, 77:48–57, jul 2014. 5

[30] R. McClung, H. Ge, J. Straube, and J. Wang. Hygrothermal performance of cross-laminated timber wall assemblies with built-in moisture: field measurements and simulations. *Building and Environment*, 71:95–110, jan 2014. 4

[31] N. Mendes. *Models for prediction of heat and moisture transfer through porous building elements*. PhD thesis, Federal University of Santa Catarina - UFSC, 1997. 4

[32] N. Mendes, M. Chhay, J. Berger, and D. Dutykh. *Numerical methods for diffusion phenomena in building physics*. PUC Press, Curitiba, Parana, 2016. 9

[33] N. Mendes, I. Ridley, R. Lamberts, P. C. Philippi, and K. Budag. Umidus: A PC program for the Prediction of Heat and Mass Transfer in Porous Building Elements. In *IBPSA 99*, pages 277–283, Japan, 1999. International Conference on Building Performance Simulation. 4

[34] A. Nayfeh. *Perturbation Methods*. Wiley-VCH, New York, 1 edition, 2000. 8

[35] W. Olek, R. Rémond, J. Weres, and P. Perré. Non-Fickian moisture diffusion in thermally modified beech wood analyzed by the inverse method. *International Journal of Thermal Sciences*, 109:291–298, nov 2016. 5

[36] S. V. Patankar. *Numerical Heat Transfer and Fluid Flow*. CRC Press, United States of America, 1980. 10, 12, 22, 27

[37] P. Perrochet and D. Bérod. Stability of the standard Crank-Nicolson-Galerkin Scheme applied to the diffusion-convection equation: Some new insights. *Water Resources Research*, 29(9):3291–3297, sep 1993. 5

[38] A. Piot, M. Woloszyn, J. Brau, and C. Abele. Experimental wooden frame house for the validation of whole building heat and moisture transfer numerical models. *Energy and Buildings*, 43(6):1322–1328, jun 2011. 5

[39] H. Rafidiarison, R. Rémond, and E. Mougel. Dataset for validating 1-D heat and mass transfer models within building walls with hygroscopic materials. *Building and Environment*, 89:356–368, jul 2015. 14

[40] J. Raphson. Analysis aequationum universalis seu adaequationes algebraicas resolvendas methodus generalis, et expedita, ex nova infinitarum serierum doctrina deducta ac demonstrata. *Microfilm copy: University Microfilms*, Ann Arbor(MI), 1690. 17

[41] C. Rode and K. Grau. Whole Building Hygrothermal Simulation Model. *ASHRAE Transactions*, 109(1):572–582, 2003. 4

[42] D. Samri. *Physical analysis and hygrothermal caracterisation of construction materials: experimental appraoch and numerical modelling*. PhD thesis, INSA de Lyon, 2008. 4

[43] D. L. Scharfetter and H. K. Gummel. Large-signal analysis of a silicon Read diode oscillator. *IEEE Transactions on Electron Devices*, 16(1):64–77, jan 1969. 11

[44] P. Talukdar, S. O. Olutmayin, O. F. Osanyintola, and C. J. Simonson. An experimental data set for benchmarking 1-D, transient heat and moisture transfer models of hygroscopic building materials. Part I: Experimental facility and material property data. *Int. J. Heat Mass Transfer*, 50(23-24):4527–4539, nov 2007. 4

[45] P. Talukdar, O. F. Osanyintola, S. O. Olutimayin, and C. J. Simonson. An experimental data set for benchmarking 1-D, transient heat and moisture transfer models of hygroscopic building materials. Part II: Experimental, numerical and analytical data. *Int. J. Heat Mass Transfer*, 50(25-26):4915–4926, dec 2007. 4

[46] F. Tariku, K. Kumaran, and P. Fazio. Transient model for coupled heat, air and moisture transfer through multilayered porous media. *Int. J. Heat Mass Transfer*, 53(15-16):3035–3044, jul 2010. 6

[47] M. Van Belleghem, M. Steeman, A. Willockx, A. Janssens, and M. De Paepe. Benchmark experiments for moisture transfer modelling in air and porous materials. *Building and Environment*, 46(4):884–898, apr 2011. 5

[48] M. Woloszyn and C. Rode. Tools for performance simulation of heat, air and moisture conditions of whole buildings. *Building Simulation*, 1(1):5–24, mar 2008. 4

J. Berger: Thermal Systems Laboratory, Mechanical Engineering Graduate Program, Pontifical Catholic University of Paraná, Rua Imaculada Conceição, 1155, CEP: 80215-901, Curitiba – Paraná, Brazil
E-mail address: Julien.Berger@pucpr.edu.br
URL: https://www.researchgate.net/profile/Julien_Berger3/

S. Gasparin: Thermal Systems Laboratory, Mechanical Engineering Graduate Program, Pontifical Catholic University of Paraná, Rua Imaculada Conceição, 1155, CEP: 80215-901, Curitiba – Paraná, Brazil
E-mail address: suelengasparin@hotmail.com
URL: https://www.researchgate.net/profile/Suelen_Gasparin/

D. Dutykh: LAMA, UMR 5127 CNRS, Université Savoie Mont Blanc, Campus Scientifique, F-73376 Le Bourget-du-Lac Cedex, France
E-mail address: Denys.Dutykh@univ-savoie.fr
URL: http://www.denys-dutykh.com/

N. Mendes: Thermal Systems Laboratory, Mechanical Engineering Graduate Program, Pontifical Catholic University of Paraná, Rua Imaculada Conceição, 1155, CEP: 80215-901, Curitiba – Paraná, Brazil
E-mail address: Nathan.Mendes@pucpr.edu.br
URL: https://www.researchgate.net/profile/Nathan_Mendes/